Phase retrieval with signal bias

Samuel T. Thurman and James R. Fienup*

The Institute of Optics, University of Rochester, Rochester, New York 14627, USA
**Corresponding author: fienup@optics.rochester.edu*

Received September 17, 2008; accepted January 27, 2009;
posted February 26, 2009 (Doc. ID 101702); published March 25, 2009

The effect of a uniform measurement bias, due to background light, stray light, detector dark current, or detector offset, on phase retrieval wavefront sensing algorithms is analyzed. Simulation results indicate that the root-mean-square error of the retrieved phase can be more sensitive to an unaccounted-for signal bias than to random noise in practical scenarios. Three methods for reducing the impact of signal bias are presented.

OCIS codes: 100.3190, 100.5070, 110.4850.

1. INTRODUCTION

Using phase retrieval, the aberrations of an imaging system can be determined from measurements of the system point spread function (PSF) [1–7]. Let $A(\xi,\eta)$ and $\phi(\xi,\eta)$ be the amplitude and phase of the generalized pupil function [8] of such a system. Under the Fresnel approximation, the three-dimensional PSF for a simple lens system is given by [8]

$$s(x,y,z) = \left| \int_{-\infty}^{\infty}\int_{-\infty}^{\infty} A(\xi,\eta)\exp[i\phi(\xi,\eta)] \times \exp\left[\frac{-i2\pi}{\lambda(d_i+z)}(\xi x+\eta y)\right] \times \exp\left[\frac{i\pi}{\lambda}\left(\frac{1}{d_o}+\frac{1}{d_i+z}-\frac{1}{f}\right)(\xi^2+\eta^2)\right] d\xi\, d\eta \right|^2, \quad (1)$$

where λ is the wavelength of light, d_o is the object distance, d_i is the image distance, f is the effective focal length of the system, and z indicates the amount of longitudinal defocus with respect to the nominal image plane. Figure 1 indicates the geometry of a simple imaging system. In this paper, the PSF measurements are modeled as

$$\tilde{s}(x,y,z_k) = s(x,y,z_k) + n(x,y,z_k) + b, \quad (2)$$

where z_k are the defocus amounts for each measurement plane, $k=\{1,2,\ldots,K\}$ is an index for the measurement planes, K is the total number of measurement planes, $n(x,y,z_k)$ is zero-mean additive noise, and b is an additive measurement bias. Bias sources include the detector offset, detector dark current, background light, and/or stray light. Typically an estimate of the bias is subtracted from the data using a dark current or dark frame subtraction method before performing phase retrieval. In Eq. (2), b represents the residual signal bias after such a dark subtraction. Given $\tilde{s}(x,y,z_k)$ and knowledge of $A(\xi,\eta)$, a phase retrieval algorithm can be used to solve the inverse problem of determining $\phi(x,\eta)$ from the PSF data.

The quality of a pupil phase estimate $\hat{\phi}(\xi,\eta)$ is affected by the bias b (in addition to being affected by random noise). Reference [9] mentions signal bias as a limiting factor for the quality of phase retrieval results. This paper examines the nature of errors in $\hat{\phi}(\xi,\eta)$ resulting from a PSF bias and methods for mitigating these errors. Section 2 describes a baseline phase retrieval algorithm optimizing a data consistency metric that does not account for a signal bias. Section 3 presents simulation results, which show that errors associated with signal bias typically occur as additional high spatial-frequency components of $\hat{\phi}(\xi,\eta)$ and that these errors can be greater than errors associated with measurement noise under realistic conditions. Additionally, physical arguments are given for the high spatial-frequency nature of the errors. Section 4 examines three methods for mitigating against these errors by (i) parameterization of $\hat{\phi}(\xi,\eta)$ as a Zernike-polynomial expansion, (ii) use of weighting functions, and (iii) use of a bias-independent data consistency metric. The advantages and disadvantages of each of these approaches are discussed. Section 5 is a summary. Portions of this paper were presented in Ref. [10].

2. BASELINE PHASE RETRIEVAL ALGORITHM

Given a particular pupil phase estimate $\hat{\phi}(\xi,\eta)$, the corresponding PSF estimates $\hat{s}(x,y,z_k)$ can be computed via a discrete form of Eq. (1) using fast Fourier transforms. The weighted normalized mean square error [11] between the modeled PSFs and the measurements can be used as a quantitative data consistency metric Φ_1, defined as

$$\Phi_1 = \frac{1}{K}\sum_k \frac{\sum_{(x,y)} w(x,y,z_k)[\alpha_k\hat{s}(x,y,z_k)-\tilde{s}(x,y,z_k)]^2}{\sum_{(x,y)} w(x,y,z_k)\tilde{s}^2(x,y,z_k)}, \quad (3)$$

where $w(x,y,z)$ is a weighting function (useful, for example, to negate the effects of bad detector pixels) and each α_k is given by

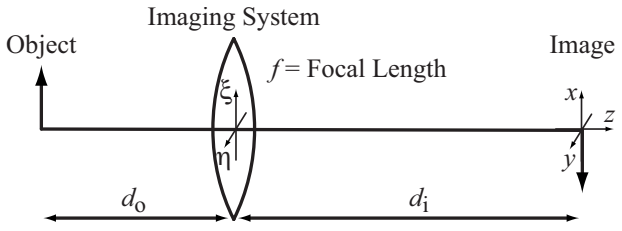

Fig. 1. Imaging system geometry.

$$\alpha_k = \frac{\sum_{(x,y)} w(x,y,z_k)\tilde{s}(x,y,z_k)\hat{s}(x,y,z_k)}{\sum_{(x,y)} w(x,y,z_k)\hat{s}^2(x,y,z_k)}, \quad (4)$$

which minimizes Φ_1 for any particular $\hat{s}(x,y,z_k)$. Note that Φ_1 accounts for an arbitrary scaling factor in the data through the α_k parameters in Eq. (3). This accommodates any changes in the detector gain, exposure time, or source intensity between PSF measurements. However, Φ_1 does not account for an arbitrary additive signal bias. $\Phi_1=1$ indicates complete disagreement between $\hat{s}(x,y,z_k)$ and $\tilde{s}(x,y,z_k)$, $\Phi_1=0$ indicates perfect agreement, while intermediate values represent the square of the normalized root-mean-square (RMS) error, e.g., $\Phi_1=0.01$ indicates 10% RMS error. The baseline phase retrieval algorithm is to use a conjugate gradient (CG) algorithm to iteratively search for the point-by-point pupil phase estimate $\hat{\phi}(\xi,\eta)$ that minimizes Φ_1 using $w(x,y,z_k)=1$.

3. ERRORS DUE TO SIGNAL BIAS

This section examines the influence of a signal bias b on the quality of the retrieved phase $\hat{\phi}(\xi,\eta)$ through numerical simulation. Figure 2 shows the pupil amplitude $A(\xi,\eta)$, phase $\phi(\xi,\eta)$, and corresponding noiseless PSFs $s(x,y,z_k)$ for the simulations. The diameter of the circular aperture represented by $A(\xi,\eta)$ was $D=50$ mm. $\phi(\xi,\eta)$ was a randomly drawn Kolmogorov phase screen [12] with piston, tip, and tilt terms subtracted and has 0.25λ RMS and 2.09λ peak-to-valley values for $\lambda=0.5$ μm. In the pupil plane there were 190 samples across the pupil diameter with a sample spacing of 0.263 mm. The two PSFs $s(x,y,z_k)$ were computed via Eq. (1) using $d_o=\infty$, $d_i=f=1200$ mm, and $z_k=\{-5,5\}$ mm, which correspond to $\pm 2.2\lambda$ peak-to-valley of defocus wavefront aberration in the pupil. The sample spacing in the PSF domain corresponds to a detector pixel pitch of $p=5$ μm, which yields a detector sampling ratio [13] of $Q=\lambda f/Dp=2.4$. Figures 2(c) and 2(d) show the center 96×96 samples of each PSF. Additionally, the PSFs were scaled such that the peak value in each measurement plane was 80,000 detected photons.

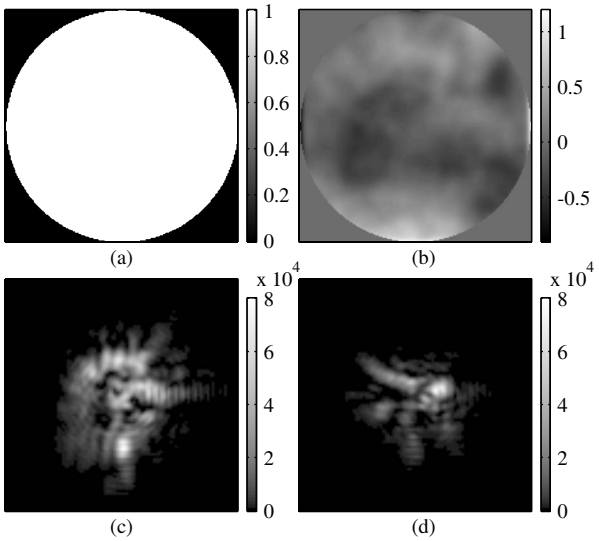

Fig. 2. Pupil function (a) amplitude $A(\xi,\eta)$ and (b) phase $\phi(\xi,\eta)$ in units of wavelength λ of imaging system used for the numerical simulations. The corresponding intensity PSFs $s(x,y,z_k)$ in front of and behind focus are shown in (c) and (d).

Phase retrieval was performed for either the case of various amounts of detector read noise (shot noise was not included) with no signal bias or no noise with various signal bias levels. The detector read noise $n(x,y,z_k)$ was zero-mean Gaussian distributed with a standard deviation of σ_r photons. The accuracy of the retrieved phase was characterized by the RMS phase error σ between $\hat{\phi}(\xi,\eta)$ and $\phi(\xi,\eta)$, ignoring any piston, tip, and tilt phase terms. Figure 3(a) is a plot of σ versus either σ_r or b, obtained by starting with the true phase as an initial estimate and running 200 iterations of a CG routine to find a point-by-point phase estimate $\hat{\phi}(\xi,\eta)$ that minimizes Φ_1.

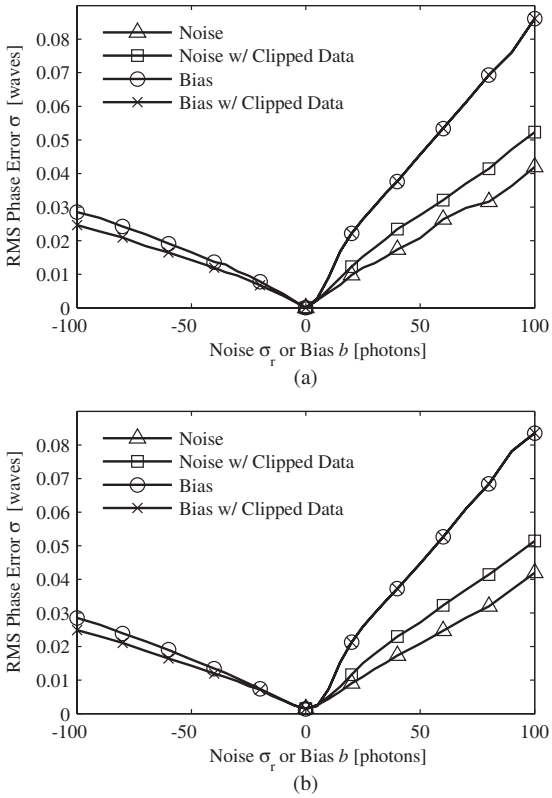

Fig. 3. RMS error in the phase retrieval results using the baseline data consistency metric Φ_1 and (triangles) different amounts of detector read noise σ_r and no signal bias, (squares) same noisy data with negative values clipped to zero, (circles) different amounts of signal bias b and no noise, and (crosses) same biased data with negative values clipped to zero. The results shown in (a) were obtained by starting the phase retrieval algorithm with the true pupil phase, while those shown in (b) were obtained starting with $\phi(\xi,\eta)=0$.

Results are shown with and without clipping negative data values (due to the noise or a negative bias) to 0. These results reflect how noise and bias displace the global minimum of Φ_1 from the true solution. Figure 3(b) shows similar results obtained by starting with zero for the initial phase estimate, retrieving a $\hat{\phi}(\xi,\eta)$ parameterized by Zernike polynomials (this approach is described in Subsection 4.A), and then running 200 CG iterations to obtain a final point-by-point phase map $\hat{\phi}(\xi,\eta)$. These results indicate the accuracy of the retrieved phase when starting with no knowledge of $\phi(\xi,\eta)$. Both graphs indicate that the RMS phase error σ increases as either σ_r or $|b|$ increases and that the quality of the retrieved phase was more sensitive to b than σ_r. The fact that the results in Fig. 3(b) are very similar to those in Fig. 3(a) indicates that, for these particular cases, phase retrieval assuming no prior knowledge of the phase was converging to the global minimum solution.

For the case with noise, clipping negative values to zero yielded poorer phase retrieval results than not clipping. For the case of negative bias, the result was better than not clipping. Presumably, both of these observations are due to a small positive bias that is introduced by asymmetrically clipping the data. For the case of positive bias, clipping had no effect since there were no negative values to clip. To put the values of σ_r and b shown in Fig. 3 into perspective, the detector gain for a 12-bit camera with a well depth of 80,000 photons is approximately 20 photons/detector count. Thus, a residual bias level of $b=5$ detector counts$=100$ photons, which represent only 0.1% of the detector dynamic range, yielded a RMS phase error $\sigma \approx \lambda/12$.

Figure 4 shows the normalized RMS error, $\sqrt{\Phi_1}$, through the solution space of $\hat{\phi}(\xi,\eta)$ along a line parameterized by

$$\hat{\phi}(\xi,\eta) = \phi(\xi,\eta) + t[\hat{\phi}_0(\xi,\eta) - \phi(\xi,\eta)], \tag{5}$$

where $\hat{\phi}_0(\xi,\eta)$ is a particular phase retrieval result and t is a scalar. Figure 4 shows the normalized RMS error along a line corresponding to $\hat{\phi}_0(\xi,\eta)$ equal to the phase retrieval result obtained by starting with the true pupil phase when $b=100$ (solid curve). When $b=0$ (dashed line), the normalized RMS error equals 0 for the true pupil phase corresponding to $t=0$. When $b=100$ photons, the true pupil phase does not correspond to a minimum of the objective function Φ_1. Consequently, the phase retrieval algorithm converges on a solution with a lower Φ_1, which corresponds to $t=1$ in the graph. The difference between the two curves shown in Fig. 4 gives some indication of how a signal bias can change the topography of the error metric over the solution space.

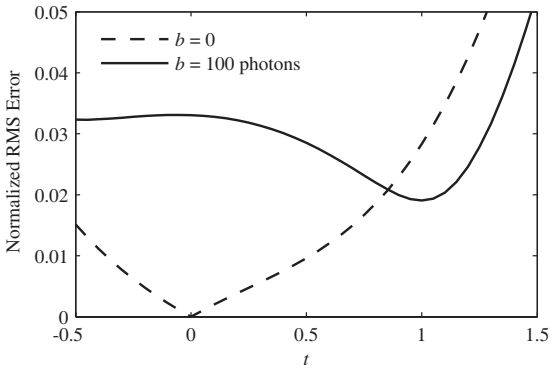

Fig. 4. Normalized RMS error, $\sqrt{\Phi_1}$, along various cuts through the phase-retrieval solution space parameterized by t through Eq. (5) for $b=0$ and 100 photons. The curves illustrate the fact that the minimum of Φ_1, which occurs at the true solution ($t=0$) for $b=0$ (dashed curve), is not a minimum for $b=100$ photons (solid curve).

Figure 5 shows the difference between the phase retrieval result $\hat{\phi}(\xi,\eta)$ and the true phase $\phi(\xi,\eta)$ for the case $b=100$ photons. Note that the phase error associated with the signal bias is composed predominantly of high spatial frequencies on the order of tens of cycles per aperture diameter. The high spatial-frequency character of this error can be understood in either the spatial or Fourier domains. In the spatial domain, an additive bias is equivalent to the addition of a large halo or intensity pedestal to each PSF. The phase retrieval algorithm introduces high spatial-frequency errors in $\hat{\phi}(\xi,\eta)$ to diffract light into this halo region and thus minimize Φ_1. Let $\tilde{S}(u,v,z_k)$ be the spatial Fourier transform of the measured PSFs $\tilde{s}(x,y,z_k)$, given by

$$\begin{aligned}\tilde{S}(u,v,z_k) &= \int_{-\infty}^{\infty}\int_{-\infty}^{\infty} \tilde{s}(x,y,z_k)\exp[-i2\pi(ux+vy)]\mathrm{d}x\mathrm{d}y \\ &= S(u,v,z_k) + N(u,v,z_k) + b\,\delta(u,v),\end{aligned} \tag{6}$$

where $S(u,v,z_k)$ (proportional to the optical transfer function) and $N(u,v,z_k)$ are the corresponding 2D Fourier transforms of $s(x,y,z_k)$ and $n(x,y,z_k)$, respectively, and $\delta(u,v)$ is a two-dimensional Dirac delta function. Note that a spatial-domain bias results in a delta function term located at the dc spatial frequency in the Fourier domain. While Φ_1 is formulated in the spatial domain, the phase retrieval algorithm essentially searches for a pupil phase such that the autocorrelation of the aberrated pupil functions matches $\tilde{S}(u,v,z_k)$. When a bias is present, the phase retrieval algorithm introduces a high spatial-

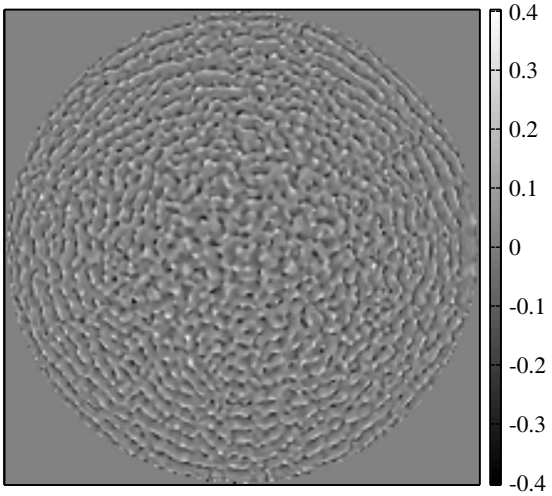

Fig. 5. High spatial-frequency error in the phase retrieval result (in units of wavelength λ) due to signal bias for $\sigma_r=0$ and $b=100$ photons.

frequency error in $\hat{\phi}(\xi,\eta)$ to reduce the autocorrelation of the defocused pupil functions for small vector displacements in an effort to match the $\delta(u,v)$ term in Eq. (6).

Figure 3 indicates that a negative bias results in a smaller phase error than does a positive bias of the same magnitude. For example, $b=-100$ photons yielded $\sigma=0.021\lambda$ while $b=100$ photons yielded $\sigma=0.056\lambda$ (when starting with zero phase). This asymmetry can be interpreted as a result of the inability of the phase retrieval algorithm to match a negative-valued halo around the measured PSFs, since modeled PSFs $\hat{s}(x,y,z_k)$ based on Eq. (1) are nonnegative. In the Fourier domain, $b<0$ can result in a $\tilde{S}(u,v,z_k)$ that is inconsistent with the Schwartz inequality, i.e., $\tilde{S}(u,v,z_k)$ may no longer be maximum at $(u,v)=0$. Hence there is no phase that will result in a PSF that agrees with a negatively biased PSF, whereas there may be a phase that yields a PSF that does at least approximately agree with a positively biased PSF. For this reason the phase retrieval algorithm is more easily lead astray by a positive bias than by a negative bias. The asymmetry in the bias effect suggests that it is better to slightly overestimate the signal bias when performing a dark subtraction than to underestimate the signal bias. The next section, however, describes more systematic approaches to mitigating the error induced by b.

4. MITIGATION APPROACHES

This section describes three approaches for reducing phase retrieval errors associated with a bias in the PSF measurements: (i) parameterization of the retrieved phase in terms of Zernike polynomials, (ii) use of weighting functions on the data, and (iii) use of a bias-independent phase retrieval metric.

A. Phase Parameterization

Often the pupil phase is dominated by low order aberrations. In such cases, it is useful to parameterize $\hat{\phi}(\xi,\eta)$ as an expansion over a set of suitable basis functions. The Zernike polynomials are an obvious choice for doing so with a circular aperture. Taking this approach, $\hat{\phi}(\xi,\eta)$ is expressed as

$$\hat{\phi}(\xi,\eta)=\sum_{j=1}^{J} c_j Z_j(\xi,\eta), \tag{7}$$

where $Z_j(\xi,\eta)$ is the jth Zernike polynomial, c_j are the expansion coefficients, $j\in\{1,2,\ldots,J\}$ is an expansion index, and J is the total number of terms included in the expansion. Instead of searching for the values of $\hat{\phi}(\xi,\eta)$ at individual samples of a point-by-point phase map in the pupil that minimize Φ_1, the phase retrieval algorithm minimizes Φ_1 with respect to the coefficients c_j. Figure 6 shows σ for this approach versus σ_r and b, for a phase parameterization using the Zernike polynomials up to and including the 30th order terms ($J=496$). These results were obtained by starting with an initial phase estimate $\hat{\phi}(\xi,\eta)=0$, running 25 CG iterations using Zernike terms up to 2nd order ($J=6$), running 25 additional iterations including 3rd order terms ($J=10$), and continuing this process of running iterations with additional terms up to

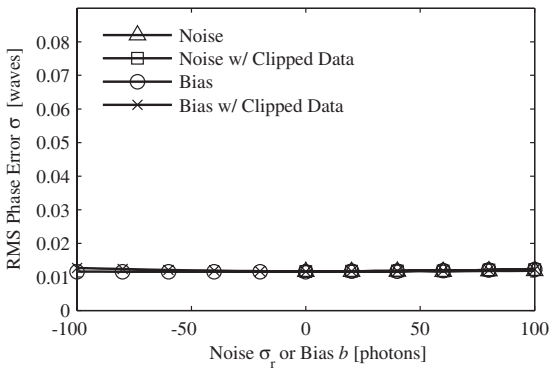

Fig. 6. Same as Fig. 3(b) except the retrieved phase was parameterized using Zernike polynomials (including terms up to 30th order).

$J=496$. Note that σ is independent of both σ_r and b, which indicates that the phase parameterization effectively mitigates against errors associated with both noise and bias for σ_r and $|b|\leq 100$ photons. A disadvantage of the phase parameterization, however, was its inability to model the full dimensionality of $\phi(\xi,\eta)$ for the simulated Kolmogorov phase screen. As a result, the expansion coefficients obtained through phase retrieval can be slightly skewed to best fit the PSF data. For example, a RMS phase error of $\sigma=0.012\lambda$ was obtained using the Zernike parameterization for the case of $\sigma_r=b=0$. This total error was evenly split between residual high spatial-frequency errors not spanned by the first 496 Zernike polynomials and errors in the estimated Zernike coefficients. Adding more terms to the phase parameterization has two benefits. First, the parameterization can better represent fine spatial details in the pupil phase, reducing the portion of σ associated with residual high spatial-frequency errors. Second, the phase retrieval algorithm generally obtains better estimates of the Zernike coefficients.

The phase parameterization generally makes the phase retrieval algorithm more robust against convergence issues. In general, one can take advantage of this benefit even when a point-by-point phase map representation of $\hat{\phi}(\xi,\eta)$ is ultimately desired. With no *a priori* knowledge of $\phi(\xi,\eta)$, one can perform phase retrieval with a parameterized phase first, to get a reasonably good estimate of $\hat{\phi}(\xi,\eta)$ without converging to a local minimum. A point-by-point phase estimate can then be obtained starting with this result. This is the approach used to achieve the results shown in Figs. 3, 7, and 8.

B. Data Weighting Function

The weighting function $w(x,y,z_k)$ in Eq. (3) is used to ignore the contribution to Φ_1 from certain portions of $\hat{s}(x,y,z_k)$. Figure 7 shows the RMS phase error σ for point-by-point phase maps $\hat{\phi}(\xi,\eta)$ obtained be minimizing Φ_1 with the following weighting:

$$w(x,y,z_k)=\begin{cases}1 & \rho<12\\ \cos^2[\pi(\rho-12)/12] & 12\leq\rho\leq 18\\ 0 & \rho>18\end{cases}, \tag{8}$$

where $\rho=\sqrt{x^2+y^2}$ is a radial spatial-domain coordinate with units of pixels. Comparing Fig. 7 with Fig. 3, it is

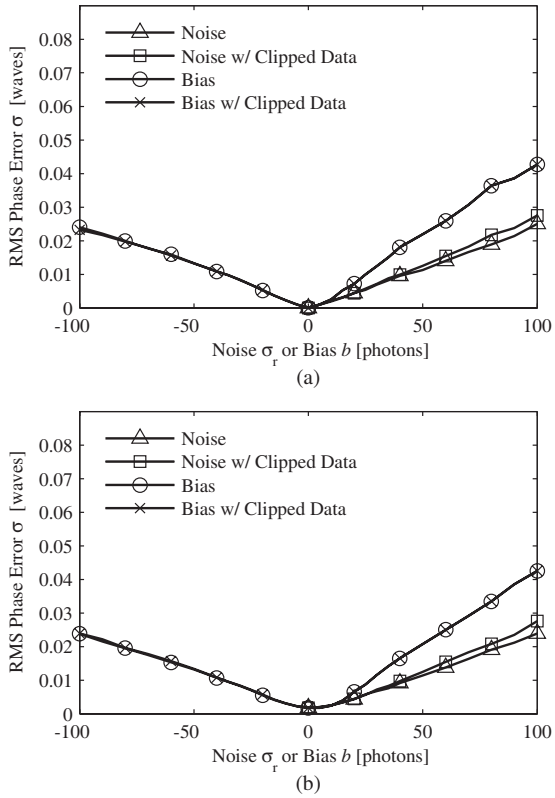

Fig. 7. Same as Fig. 3 except the weighting function $w(x,y,z_k)$ defined by Eq. (8) was used to ignore data outside the bright portion of each PSF.

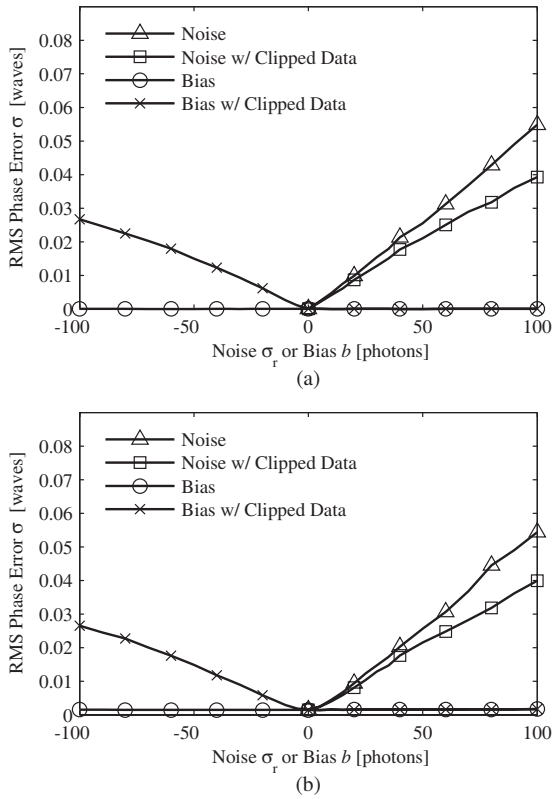

Fig. 8. Same as Fig. 3 except the bias-independent metric Φ_2 was used in the phase retrieval algorithm.

evident the use of $w(x,y,z_k)$ significantly reduces the impact of both σ_r and b on the quality of the phase retrieval results. The results shown in Fig. 7 were obtained with 200 CG iterations minimizing Φ_1, starting with either the true pupil phase $\phi(\xi,\eta)$ or the polynomial phase estimates $\hat{\phi}(\xi,\eta)$ obtained in Subsection 4.A.

The form of Eq. (8) was chosen to yield $w(x,y,z_k)=1$ in a region a bit larger than the visible extent of the PSFs shown in Figs. 2(c) and 2(d) and $w(x,y,z_k)=0$ in the region where the PSFs are near zero, with a smooth transition from $w(x,y,z_k)=1$ to $w(x,y,z_k)=0$. The phase retrieval algorithm ignores data at detector pixels where $w(x,y,z_k)=0$. Note that this is not the same as setting the PSF data to zero and seeking a phase that matches the resulting PSF. For minimizing the impact of σ_r, this is a good choice for $w(x,y,z_k)$ since the signal-to-noise ratio is poorest in the regions surrounding each PSF. Additionally, this is a good choice for minimizing the impact of b, since it limits the extent of the bias "halo" surrounding each PSF to the region where $w(x,y,z_k)>0$.

C. Bias-Independent Metric

Metric Φ_1, given by Eq. (3), accounts for different multiplicative scaling factors α_k between the measured PSFs. As mentioned above, these scaling differences originate from changes in the detector exposure time, gain setting, or source intensity. Each PSF measurement can also have an additive bias β_k due to dark current accumulated throughout the exposure, detector offset, or stray light. In this paper, the bias b included in the simulated data via Eq. (2) is the same for each PSF measurement. A new data consistency metric Φ_2 can be defined to account for an arbitrary additive signal bias as well as a scaling factor. Such a metric is given by

$$\Phi_2 = \frac{1}{K}\sum_k \frac{\sum_{(x,y)} w(x,y,z_k)[\alpha_k \hat{s}(x,y,z_k) + \beta_k - \tilde{s}(x,y,z_k)]^2}{\sum_{(x,y)} w(x,y,z_k)\tilde{s}^2(x,y,z_k)}, \tag{9}$$

where α_k and β_k are chosen to minimize Φ_2. Solving for the β_k that yields $\partial\Phi_2/\partial\beta_k=0$ yields

$$\beta_k = \frac{\sum_{(x,y)} w(x,y,z_k)[\tilde{s}(x,y,z_k) - \alpha_k \hat{s}(x,y,z_k)]}{\sum_{(x,y)} w(x,y,z_k)}. \tag{10}$$

Substituting Eq. (10) into Eq. (9) yields

$$\Phi_2 = \frac{1}{K}\sum_k \frac{\sum_{(x,y)} w(x,y,z_k)[\alpha_k \hat{g}(x,y,z_k) - \tilde{g}(x,y,z_k)]^2}{\sum_{(x,y)} w(x,y,z_k)\tilde{s}^2(x,y,z_k)}, \tag{11}$$

where

$$\hat{g}(x,y,z_k) = \hat{s}(x,y,z_k) - \frac{\sum_{(x,y)} w(x,y,z_k)\hat{s}(x,y,z_k)}{\sum_{(x,y)} w(x,y,z_k)}, \quad (12)$$

$$\tilde{g}(x,y,z_k) = \tilde{s}(x,y,z_k) - \frac{\sum_{(x,y)} w(x,y,z_k)\tilde{s}(x,y,z_k)}{\sum_{(x,y)} w(x,y,z_k)}. \quad (13)$$

The desired value of α_k is obtained by solving $\partial\Phi_2/\partial\alpha_k = 0$ to yield

$$\alpha_k = \frac{\sum_{(x,y)} w(x,y,z_k)\tilde{g}(x,y,z_k)\hat{g}(x,y,z_k)}{\sum_{(x,y)} w(x,y,z_k)\hat{g}^2(x,y,z_k)}. \quad (14)$$

Inserting this expression into Eq. (11) and simplifying yields

$$\Phi_2 = \frac{1}{K}\sum_k \left[\sum_{(x,y)} w(x,y,z_k)\tilde{s}^2(x,y,z_k)\right]^{-1} \times \left\{\left[\sum_{(x,y)} w(x,y,z_k)\tilde{g}^2(x,y,z_k)\right] - \left[\sum_{(x,y)} w(x,y,z_k)\hat{g}^2(x,y,z_k)\right]^{-1} \times \left[\sum_{(x,y)} w(x,y,z_k)\tilde{g}(x,y,z_k)\hat{g}(x,y,z_k)\right]^2\right\}. \quad (15)$$

Figure 8 shows the RMS phase error σ obtained using Φ_2 versus σ_r and b with $w(x,y,z_k)=1$. These results were obtained after 200 CG iterations, starting with an initial phase estimate equal to (a) the true pupil phase or (b) the parameterized phase retrieval results of Subsection 4.A. This second starting condition is based on the strategy of using a phase parameterization to find an approximate solution while avoiding problems with local minima and then using a point-by-point representation to obtained a more detailed phase estimate. Note that the phase retrieval results are independent of the value of the signal bias b, except when negative data values are clipped to 0, which produces errors in the PSF measurements. The effects of clipping are complicated by the fact that clipping can introduce signal-dependent errors into the PSF measurements by selectively clipping negative values when the signal bias is negative. When applied to an array of zero-mean noise, clipping reduces the noise variance by eliminating all of the negative values but causes the noise to have a positive mean value. Presumably clipping yielded better results with noisy data because the clipping reduces the standard deviation of the read noise, and Φ_2 ignores any induced bias. Comparing Figs. 3 and 8, it seems that the results using Φ_2 are slightly more sensitive to the noise level σ_r in some cases than are the results using Φ_1. One possible reason for this is that the phase retrieval algorithm can better fit the texture of the zero-mean noise in $\tilde{s}(x,y,z_k)$ in the region surrounding each PSF with a nonnegative computed PSF by assuming a negative bias β_k. Figure 9 supports this hypothesis. The plot shows the value of β_k given by Eq. (10) for each plane of data versus σ_r. The figure indicates that the phase retrieval algorithm tended to include a negative additive bias β_k, of which the magnitude increases with the amount of read noise.

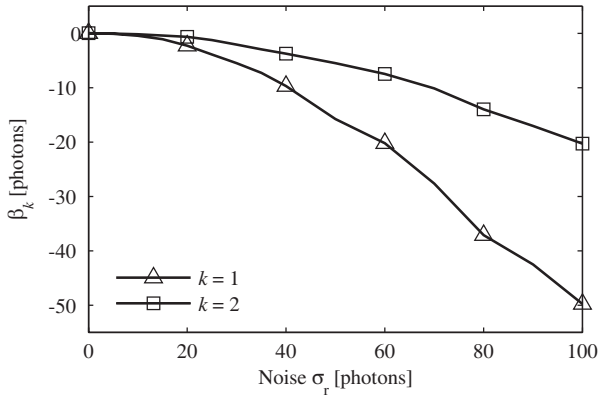

Fig. 9. Estimated signal bias values β_k versus the amount of read noise σ_r corresponding to the results shown in Fig. 8(b) for both the $k=1$ and the $k=2$ planes of data.

5. SUMMARY

Dark subtraction techniques can be used to remove a signal bias from PSF measurements used for phase retrieval. Numerical simulations, however, indicate that small amounts of residual bias remaining in the measurements can degrade the quality of phase retrieval results. Numerical simulation results indicate that the RMS error in the phase retrieved using the baseline algorithm is about a factor of two more sensitive to the amount of residual signal bias than the same amount of detector read noise. The phase error induced by a signal bias is composed predominantly of high spatial frequencies, since such errors can produce a halo of energy outside the bright area of the true PSF. Three approaches for effectively mitigating the effect of signal bias were examined: (i) parameterizing the retrieved phase in terms of Zernike polynomials, (ii) use of a data weighting function, and (iii) use of bias-independent data consistency metric. All three approaches reduced the errors due to the bias. The phase parameterization can introduce errors if the number of phase terms does not adequately describe the true solution, and the bias-independent metric is a bit more sensitive to noise than a standard data consistency metric, but this is very effective when the bias error dominates.

ACKNOWLEDGMENT

This work was funded by NASA Goddard Space Flight Center.

REFERENCES

1. R. W. Gerchberg and W. O. Saxton, "A practical algorithm for the determination of the phase from image and diffraction plane pictures," Optik (Stuttgart) **35**, 237–246 (1972).

2. D. L. Misell, "A method for the solution of the phase problem in electron microscopy," J. Phys. D **6**, L6–L9 (1973).
3. R. A. Gonsalves, "Phase retrieval and diversity in adaptive optics," Opt. Eng. (Bellingham) **21**, 829–832 (1982).
4. J. N. Cederquist, J. R. Fienup, C. C. Wackerman, S. R. Robinson, and D. Kryskowski, "Wave-front phase estimation from Fourier intensity measurements," J. Opt. Soc. Am. A **6**, 1020–1026 (1989).
5. J. R. Fienup, "Phase-retrieval algorithms for a complicated optical system," Appl. Opt. **32**, 1737–1746 (1993).
6. J. R. Fienup, J. C. Marron, T. J. Schulz, and J. H. Seldin, "Hubble Space Telescope characterized by using phase-retrieval algorithms," Appl. Opt. **32**, 1747–1767 (1993).
7. C. Roddier and F. Roddier, "Combined approach to Hubble Space Telescope wave-front distortion analysis," Appl. Opt. **32**, 2992–3008 (1993).
8. J. W. Goodman, *Introduction to Fourier Optics*, 3rd ed. (Roberts, 2005).
9. N. J. Miller, M. P. Dierking, and B. D. Duncan, "Optical sparse aperture imaging," Appl. Opt. **46**, 5933–5943 (2007).
10. S. T. Thurman and J. R. Fienup, "Systematic phase retrieval error due to signal bias," in *Frontiers in Optics*, OSA Technical Digest (CD) (Optical Society of America, 2006), paper FTuY4.
11. J. R. Fienup, "Invariant error metrics for image reconstruction," Appl. Opt. **36**, 8352–8357 (1997).
12. R. G. Lane, A. Glindemann, and J. C. Dainty, "Simulation of a Kolmogorov phase screen," Waves Random Media **2**, 209–224 (1992).
13. R. D. Fiete, "Image quality and λ FN/p for remote sensing systems," Opt. Eng. (Bellingham) **38**, 1229–1240 (1999).